

Energetics of a Single Qubit Gate

J. Stevens,^{1,*} D. Szombati,^{1,*} M. Maffei,² C. Elouard,³ R. Assouly,¹ N. Cottet,¹ R. Dassonneville,¹
Q. Ficheux,¹ S. Zeppetzauer,¹ A. Bienfait,¹ A. N. Jordan,^{4,5} A. Auffèves,² and B. Huard¹

¹*Univ Lyon, ENS de Lyon, CNRS, Laboratoire de Physique, F-69342 Lyon, France*

²*CNRS and Université Grenoble Alpes, Institut Néel, F-38042 Grenoble, France*

³*QUANTIC team, INRIA de Paris, 2 Rue Simone Iff, 75012 Paris, France*

⁴*Institute for Quantum Studies, Chapman University, 1 University Drive, Orange, CA 92866, USA*

⁵*Department of Physics and Astronomy, University of Rochester, Rochester, New York 14627, USA*

(Dated: September 21, 2021)

Qubits are physical, a quantum gate thus not only acts on the information carried by the qubit but also on its energy. What is then the corresponding flow of energy between the qubit and the controller that implements the gate? Here we exploit a superconducting platform to answer this question in the case of a quantum gate realized by a resonant drive field. During the gate, the superconducting qubit becomes entangled with the microwave drive pulse so that there is a quantum superposition between energy flows. We measure the energy change in the drive field conditioned on the outcome of a projective qubit measurement. We demonstrate that the drive's energy change associated with the measurement backaction can exceed by far the energy that can be extracted by the qubit. This can be understood by considering the qubit as a weak measurement apparatus of the driving field.

Quantum gates have an energetic cost that may limit the performances of future quantum computers [1–4]. Understanding the flows of energy during a single qubit gate is of prime importance in this context. Since it is possible for a gate to prepare a quantum superposition of states with different energies, the energy balance between the gate controller and the qubit can be seen as a quantum superposition of energetic costs. Focusing on gates performed by resonant drives, the drive appears to have exchanged energy with the qubit, yet the amount of transferred energy is undetermined until the qubit state is measured. How is the energy in the driving mode modified by the qubit measurement and what does it reveal about the joint qubit-drive system? Superconducting circuits offer a state-of-the-art platform for exploring this question owing to the possibility to perform single shot qubit readout using an ancillary cavity and quantum-limited measurements of propagating microwave modes [5]. In particular, it is possible to manipulate [6–9] and probe [10–13] the fields interacting resonantly with the qubit. Correlations between the resonant drive amplitude and the outcome of a later qubit measurement have been evidenced by probing quantum trajectories of superconducting qubits [14–18] including when a projective measurement is used to perform post-selection [19–21]. However the demonstration of correlations between the energy of the drive mode and the qubit state is missing.

In this Letter, we present an experiment in which we directly probe the energy in the driving mode conditioned on the measured qubit state. We observe that measuring the qubit energy leads to a change in the energy of the driving pulse owing to its entanglement with the qubit before measurement. Strikingly, we also observe that the energy of the pulse can change by more than a quantum depending on the measured qubit state, revealing a subtle

backaction of the qubit measurement on the drive pulse.

In order to better understand the rise of these correlations, let us consider the joint evolution of the qubit and drive mode during the qubit gate. Assuming the qubit starts in the ground state $|g\rangle$, and is driven by a coherent state $|\psi_{\text{in}}\rangle$, the qubit and the propagating drive mode a are initially in the separable state $|\psi_{\text{in}}\rangle \otimes |g\rangle$ (see Fig. 1a). Owing to the light-matter coupling between the drive mode and the qubit, they evolve into the entangled state [15, 23]

$$\lambda_g |\psi_g\rangle \otimes |g\rangle + \lambda_e |\psi_e\rangle \otimes |e\rangle \quad (1)$$

where λ_g and λ_e are the probability amplitudes for each state in the superposition, and $|\psi_{g,e}\rangle$ designate the outgoing states of the drive mode (see Fig. 1b). Note that these parameters and states depend on $|\psi_{\text{in}}\rangle$ implicitly. The qubit gate is parametrized by the rotation of angle θ undergone by the qubit Bloch vector, revealed by tracing over the field degrees of freedom. Interestingly, the entanglement above limits the fidelity of a qubit gate [1–4] since the purity of the qubit density matrix ρ reads

$$\text{tr}(\rho^2) = 1 - 2|\lambda_g \lambda_e|^2 (1 - |\langle \psi_e | \psi_g \rangle|^2). \quad (2)$$

Luckily for quantum information processing, the overlap between $|\psi_g\rangle$ and $|\psi_e\rangle$ tends to 1 as the drive amplitude increases [24]. The lack of purity also determines how much information can be extracted about the drive mode when measuring the qubit state. From an energetics point of view, when the qubit is measured in its energy basis, the measurement backaction prepares the drive mode in states of different energy expectations. Conservation of the expected energy before and after the resonant interaction leads to the following equality relating the expected number of quanta in the initial state

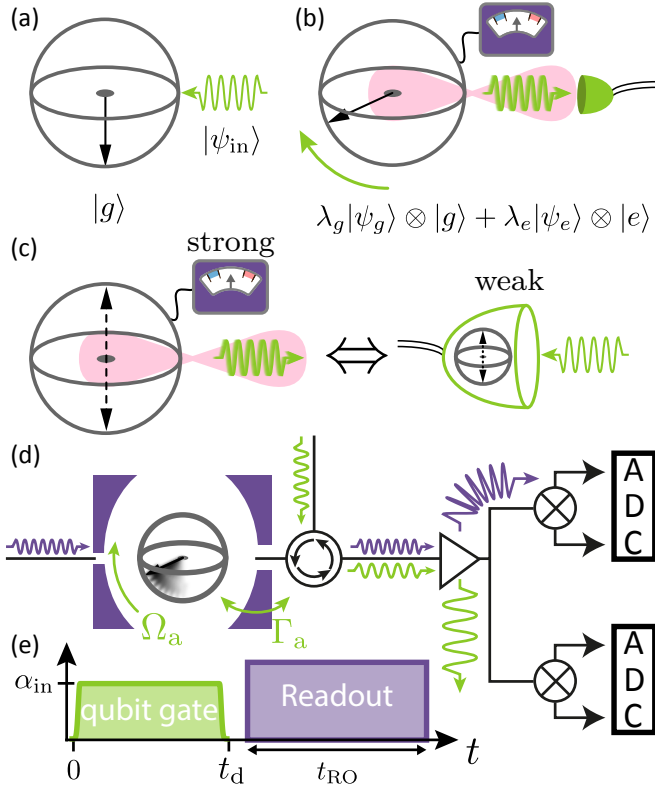


FIG. 1. Principle of the experiment. a. Coherent wavepacket $|\psi_{\text{in}}\rangle$ (green arrow) at the qubit frequency interacts with a qubit prepared in $|g\rangle$ (Bloch vector). b. Resulting entangled state Eq. (1). The energy of the outgoing drive wavepacket is measured and averaged conditionally on the outcome of a strong readout of the qubit energy. c. Schematics highlighting the equivalence between the action of the projective qubit measurement and that of a weak measurement apparatus on the pulse. d. The transmon qubit is placed inside a microwave cavity (purple) to perform its readout by sending a pulse at the cavity frequency through a weakly coupled port (left). The resonant field (green) addressing the qubit is sent through a strongly coupled port on the right. Both pulses exit through this port and are directed by a circulator into low noise amplifiers. Their quadratures are measured via two heterodyne setups based on Analog-to-Digital Converters (ADCs) operating at qubit and cavity frequencies. e. Scheme of the experimental pulse sequence, where $t_d = 400$ ns and $t_{\text{RO}} = 704$ ns [22].

$|\psi_{\text{in}}\rangle \otimes |g\rangle$ and the final state (1)

$$\langle a^\dagger a \rangle_{|\psi_{\text{in}}\rangle} = |\lambda_g|^2 \langle a^\dagger a \rangle_{|\psi_g\rangle} + |\lambda_e|^2 [\langle a^\dagger a \rangle_{|\psi_e\rangle} + 1]. \quad (3)$$

However, the two terms in the superposition (1) are counterintuitively not required to have the same energy and thus $|\psi_g\rangle$ and $|\psi_e\rangle$ may differ by more than a quantum of energy at the qubit frequency. In this work, we directly measure the energy contained in the states $|\psi_g\rangle$ and $|\psi_e\rangle$, and its dependence on the drive amplitude. Interestingly, from the point of view of the driving mode, the qubit acts as a weak measurement apparatus, which

exerts a backaction that our experiment is able to probe (Fig. 1c).

Our setup is schematically represented in Fig. 1d [22]. A transmon qubit of frequency $\omega_Q = 2\pi \times 4.81$ GHz is embedded in a superconducting cavity of frequency $\omega_R = 2\pi \times 7.69$ GHz below 15 mK. The qubit relaxation time $T_1 = 5.5 \pm 0.3$ μs is mainly limited by its coupling rate $\Gamma_a/2\pi = 20$ kHz to a transmission line that carries the driving mode a . The qubit pure dephasing time is $T_\phi = 2.4$ μs .

We perform the following experiment. First, a pulse of varying amplitude α_{in} , whose phase is chosen so that $\alpha_{\text{in}} > 0$, drives the qubit at frequency ω_Q for a fixed duration $t_d = 400$ ns (Fig. 1e). The pulse is reflected and amplified using a Travelling Wave Parametric Amplifier (TWPA) [25]. A heterodyne measurement yields a continuous record of its two quadratures. This drive pulse induces a rotation of the qubit of angle θ around σ_y . The qubit is then measured dispersively 20 ns later using a 704 ns-long pulse at the cavity frequency ω_R sent on a weakly-coupled auxiliary port. This readout pulse exits through the strongly coupled output port used for driving the qubit and its transmission is detected through the same amplification chain.

We start by measuring the average energy in the reflected drive pulse. From the heterodyne measurement it is possible to access both the complex amplitude α_m and the instantaneous outgoing power \dot{n}_m (in units of photons per second) referred to the qubit output port [22]. To account for the added noise of the amplifiers and possible experimental gain drifts, we interleave the measurement with a calibration sequence. The average measured photon rate outgoing from the qubit in state ρ is given by [26–28]

$$\overline{\dot{n}_m}^\rho = \alpha_{\text{in}}^2 - \frac{\Omega_a}{2} \langle \hat{\sigma}_x \rangle_\rho + \Gamma_a \frac{1 + \langle \hat{\sigma}_z \rangle_\rho}{2} \quad (4)$$

where $\Omega_a = 2\sqrt{\Gamma_a}\alpha_{\text{in}}$ is the Rabi frequency. In Fig. 2a, we show the evolution of $\overline{\dot{n}_m}^\rho$ for varying input drive powers. This measurement is the temporal version of the Mollow triplet, which was already observed in several experiments [10–13].

To extract the correlation between the power of the re-emitted microwave drive and final qubit state, we average the instantaneous power conditioned on the measured qubit state (Fig. 2). We observe that a clear deviation exists from the unconditional average power. Theoretically, it is possible to capture the dependence of the drive power on qubit measurement outcome using the past quantum state formalism [29–31]. A full description of the drive mode at each moment in time can be given by considering both the initial starting condition via the density matrix of the qubit $\rho(t)$ and the final measurement result through the effect matrix of the qubit $E(t)$. The density matrix obeys the standard Lindblad equation while the effect matrix is constrained by its value at

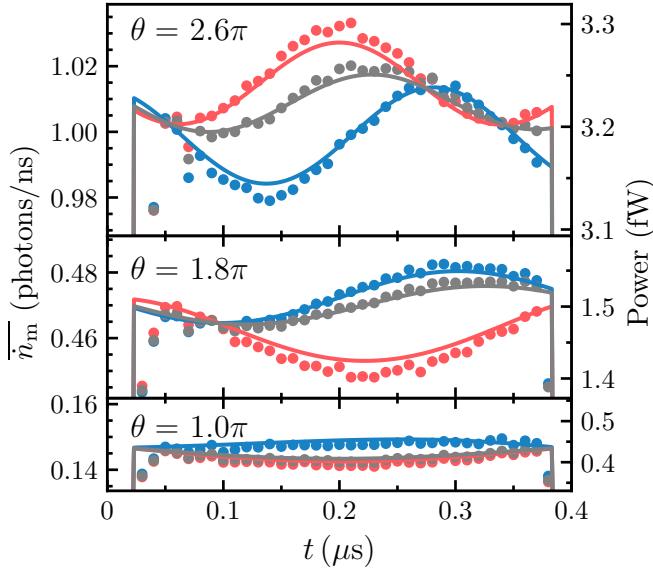


FIG. 2. Measured power of the reflected drive. Dots: mean instantaneous power \bar{n}_m of the outgoing drive in units of photon flux [22] as a function of time t . Each panel corresponds to a different input drive amplitude resulting in qubit rotation angles $\theta = \pi, 1.8\pi$ and 2.6π . Gray: averaging without post-selection, blue (red): averaging conditioned on the qubit being measured in $|g\rangle$ ($|e\rangle$). Lines: expected power from Eq. (6). The time delay between the experimental and numerical data has been adjusted by hand.

the final measurement time and is back propagated using the adjoint of the Lindblad equation (see [22]). This formalism was used in Ref. [19] in order to determine the post-selected average evolution of the transmitted drive amplitude through a qubit. For a reflected drive, the post-selected average measured drive amplitude reads

$$\overline{\alpha}_m^{E,\rho} = \alpha_{in} - \sqrt{\Gamma_a} \operatorname{Re}[_E\langle\hat{\sigma}_-\rangle_\rho], \quad (5)$$

where $_E\langle\hat{\sigma}_-\rangle_\rho = \frac{\operatorname{Tr}[E(t)\hat{\sigma}_-\rho(t)]}{\operatorname{Tr}[E(t)\rho(t)]}$ is the weak value of the qubit lowering operator $\hat{\sigma}_- = (\hat{\sigma}_x - i\hat{\sigma}_y)/2$. The coherent part of the power emitted by the qubit corresponds to the modulus square of that amplitude. In contrast, in this work we are concerned with the total energy contained in the drive mode, and not only the coherent part. One can show that the post-selected expectation value of the outgoing photon rate is given by [32, 33]

$$\overline{\dot{n}}_m^{E,\rho} = |\alpha_{in}|^2 - \Omega_a \operatorname{Re}[_E\langle\hat{\sigma}_-\rangle_\rho] + \Gamma_a \mathcal{I}(E, \rho), \quad (6)$$

where $\mathcal{I}(E, \rho) = \frac{\operatorname{Tr}[E\hat{\sigma}_-\rho\hat{\sigma}_+]}{\operatorname{Tr}[E\rho]}$ can be understood as the weak value of a photo-detection rate. To compute Eq. (6), we solve the forward and backward Lindblad equations. An independent measurement allows us to set $\rho(0)$ to a thermal state with an excitation probability $p_e^{\text{th}} = 0.088 \pm 0.002$. The effect matrix E is set at measurement time $t = t_d$ conditionally on the post-selected

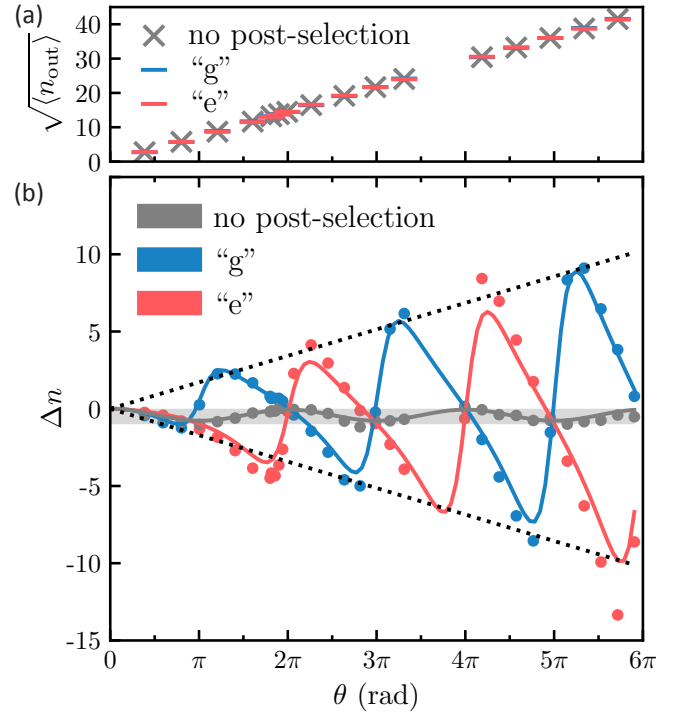


FIG. 3. a. Square root of the measured total mean number of photons in the outgoing drive pulse as a function of the qubit rotation angle θ around $\hat{\sigma}_y$ for post-selected and non post-selected data. For these photon numbers, the effect of post-selection is almost indistinguishable. b. Dots: measured difference Δn between the mean post-selected number of photons and the mean number of photons in the incoming drive pulse as a function of the qubit rotation angle. Colors indicate the kind of post-selection. Lines: time integrated Eq. (6). Dotted lines: guides to the eye scaling with $\theta \propto \sqrt{n_{in}}$. Shaded area: allowed range of exchanged energy without post-selection (between -1 and 0 photons).

readout outcome. When the qubit is measured in state $|e\rangle$ with a readout fidelity $F_e = 0.867 \pm 0.028$, it is given by $E_e(t_d) = F_e |e\rangle\langle e| + (1 - F_e) |g\rangle\langle g|$, while, when the qubit is measured in state $|g\rangle$ with a readout fidelity $F_g = 0.985 \pm 0.015$, it is $E_g(t_d) = F_g |g\rangle\langle g| + (1 - F_g) |e\rangle\langle e|$ [22]. Note that without post-selection, the effect matrix is the identity and Eq. (6) comes down to the non post-selected case in Eq. (4). The Eq. (6) reproduces the measured post-selected instantaneous powers we observe (solid lines Fig. 2b), where the single fit parameter is the electrical delay of the setup.

Our original motivation is to quantify the difference of energy between the post-selected drive pulses. We thus now look at the total number of photons contained in the pulse. It can be calculated as $\langle n_{out} \rangle = \int_0^{t_d} \overline{\dot{n}}_m^{E,\rho} dt$ from the experimental data. In Fig. 3a, we show the square root of the measured total photon numbers $\sqrt{\langle n_{out} \rangle}$ as a function of the rotation angle θ in the Bloch sphere. The photon number scales as the square of the rotation angle as expected since the Rabi frequency scales as the drive

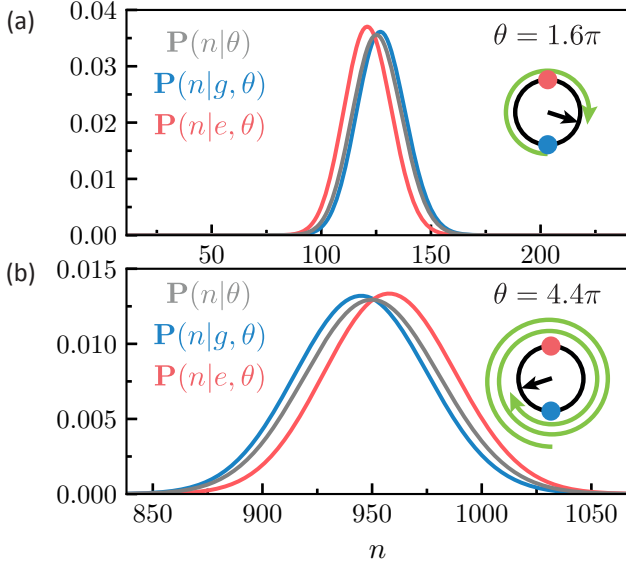


FIG. 4. Probability distribution that the drive pulse contains n photons knowing that it was prepared in a coherent state leading to a Rabi rotation of $\theta = 1.6\pi$ (a) or $\theta = 4.4\pi$ (b). Colors encode the post-selected outcome of the qubit measurement: no post-selection (grey), $|g\rangle$ (blue) and $|e\rangle$ (red). Insets: Bloch representation of the qubit state after the drive pulse has left it. Green arrow: Rabi rotation. Blue and red dots: $|g\rangle$ and $|e\rangle$ states.

amplitude. The observed difference between $\langle n_{\text{out}} \rangle$ for both qubit measurement outcomes is negligible compared to the total number of photons in the pulse, as expected from the strong overlap of states $|\psi_g\rangle$ and $|\psi_e\rangle$.

To reveal the difference between the energies of these states, we thus subtract the mean number of photons contained in the incoming pulse $n_{\text{in}} = \int_0^{t_d} |\alpha_{\text{in}}(t)|^2 dt$ (Fig. 3b). Without post-selection, the difference $\Delta n = \langle n_{\text{out}} \rangle - n_{\text{in}}$ oscillates between -1 and 0 , as expected from the principle of energy conservation: when the qubit is excited, it extracts a photon from the pulse and when it is in the ground state the pulse energy stays unchanged. As commonly observed with weak value measurements, the oscillation amplitudes of the post-selected $\Delta n_{g,e}$ can exceed the non post-selected amplitude (blue and red dots compared to shaded area in Fig. 3b) [34]. The post-selected photon number Δn_g oscillates in counter-phase with Δn_e : the information acquired on the qubit state distorts the probability of finding a given photon number in the drive pulse.

To give a better insight into the effect of the qubit measurement on the photon distribution, we consider a toy model where the drive pulse is modeled as a stationary harmonic oscillator, which interacts with a decoherence free qubit for a time t_d at a fixed rate Γ_a . A complete description would treat the drive pulse as a propagating field [32, 35] and yields identical results. The oscillator starts in a coherent state $|\sqrt{n_{\text{in}}}\rangle = |\theta/\sqrt{4\Gamma_a t_d}\rangle$

with a Poisson distribution $\mathbf{P}_\theta(n)$ for the photon number centered on n_{in} (grey lines in Fig. 4). Post-selecting on a particular qubit measurement outcome distorts this probability distribution. The measurement operators \hat{M}_g and \hat{M}_e describing the backaction exerted on the oscillator when the qubit is measured in $|g\rangle$ or in $|e\rangle$ read $\hat{M}_g = \cos(\sqrt{4\Gamma_a t_d} \hat{a}^\dagger \hat{a})$ and $\hat{M}_e = \hat{e} \sin(\sqrt{4\Gamma_a t_d} \hat{a}^\dagger \hat{a})$, where $\hat{e} = \sum_n |n\rangle \langle n+1|$ is the bare lowering operator (see [22]). Inspired by the problem of photodetection of a cavity output [22], we distinguish two effects in the backaction: (i) the Bayesian update on the photon distribution conditioned on the measurement outcome and (ii) the extraction of a single photon from the drive pulse which is used to flip the qubit into its excited state.

Through (i), the Poisson distribution are multiplied by $\langle n | \hat{M}_i^\dagger \hat{M}_i | n \rangle$, which is either $\cos^2(\sqrt{n\Gamma_a t_d})$ or $\sin^2(\sqrt{n\Gamma_a t_d})$, and then renormalized (see section 9 in [22]). This Bayesian update leads to an increase or a decrease of the mean occupancy. The direction depends on the rotation angle since the outcome of the qubit measurement indicates that the qubit is either ahead of its average evolution (more photons than expected in the drive), or behind (less photons). One can see that for $\theta = 1.6\pi$, finding the qubit in $|g\rangle$ projects it ahead of its average evolution and thus offsets the probability distribution $\mathbf{P}_\theta(n|g)$ towards larger photon numbers. Each half turn, the situation reverses, explaining why for $\theta = 4.4\pi$, $\mathbf{P}_\theta(n|g)$ is offset towards smaller photon numbers. This behavior explains the oscillations we observe in Fig. 3. Moreover, owing to the increasing standard deviation of the Poisson distribution $\mathbf{P}_\theta(n)$ with the amplitude $\sqrt{n_{\text{in}}} \propto \theta$, the backaction on Δn increases linearly with θ (dotted lines in Fig. 3b and [22]).

Through (ii), the qubit measurement backaction entails the destruction of a photon in the drive pulse when the qubit is found in $|e\rangle$ and no extra cost when in $|g\rangle$. This single photon offset corresponds to the operator \hat{e} in \hat{M}_e and amounts to the minimum of the measured oscillations in the non post-selected average Δn . For the post-selected cases, this contribution of the measurement backaction is not immediately visible in the measured $\Delta n_{g,e}$, but can be made explicit in the predicted oscillations derived from the past quantum state model of Fig. 3b (see [22]).

In conclusion, we measured the energy flows between a qubit and the resonant drive often used to perform single-qubit gates. The unavoidable entanglement between the qubit and the drive reflects on an observable energy exchange. In this context, the projective measurement of the qubit can be understood as a weak measurement of the drive pulse. The energy change of the drive pulse after the qubit measurement can exceed the maximal qubit extracted energy of one photon. While surprising when considering the average experiment, it is well explained by a weak-value model. Looking forward, it would be

interesting to perform a full quantum tomography of the drive state using newly-developed itinerant mode detectors [36, 37] by first displacing the quantum state towards low photon numbers. From a thermodynamic point of view, this measurement backaction on the energy could be used to build new thermodynamic engines that are powered by measurement [38–50].

This research was supported by grant number FQXi-IAF19-05 from the Foundational Questions Institute Fund, a donor advised fund of Silicon Valley Community Foundation; the Templeton World Charity Foundation, Inc (Grant No. TWCFO338), the ANR Research Collaborative Project "Qu-DICE" (ANR-PRC-CES47) and the John Templeton Foundation grant no. 61835. We acknowledge IARPA and Lincoln Labs for providing a Josephson Traveling-Wave Parametric Amplifier.

* These authors have contributed equally.

- [1] J. Gea-Banacloche, Some implications of the quantum nature of laser fields for quantum computations, *Physical Review A* **65**, 022308 (2002).
- [2] J. Gea-Banacloche, Minimum Energy Requirements for Quantum Computation, *Physical Review Letters* **89**, 217901 (2002).
- [3] M. Ozawa, Conservative Quantum Computing, *Physical Review Letters* **89**, 057902 (2002).
- [4] J. Ikonen, J. Salmilehto, and M. Möttönen, Energy-efficient quantum computing, *npj Quantum Information* **3**, 1 (2017).
- [5] X. Gu, A. F. Kockum, A. Miranowicz, Y.-x. Liu, and F. Nori, Microwave photonics with superconducting quantum circuits, *Physics Reports Microwave photonics with superconducting quantum circuits*, **718-719**, 1 (2017).
- [6] A. A. Houck, D. I. Schuster, J. M. Gambetta, J. A. Schreier, B. R. Johnson, J. M. Chow, L. Frunzio, J. Majer, M. H. Devoret, S. M. Girvin, and R. J. Schoelkopf, Generating single microwave photons in a circuit, *Nature* **449**, 328 (2007).
- [7] I.-C. Hoi, C. M. Wilson, G. Johansson, T. Palomaki, B. Peropadre, and P. Delsing, Demonstration of a Single-Photon Router in the Microwave Regime, *Physical Review Letters* **107**, 073601 (2011).
- [8] I.-C. Hoi, T. Palomaki, J. Lindkvist, G. Johansson, P. Delsing, and C. M. Wilson, Generation of Nonclassical Microwave States Using an Artificial Atom in 1D Open Space, *Physical Review Letters* **108**, 263601 (2012).
- [9] K. Reuer, J.-C. Besse, L. Wernli, P. Magnard, P. Kurpiers, G. J. Norris, A. Wallraff, and C. Eichler, Realization of a Universal Quantum Gate Set for Itinerant Microwave Photons, *arXiv:2106.03481 [quant-ph]* (2021).
- [10] O. Astafiev, A. M. Zagoskin, A. A. Abdumalikov, Y. A. Pashkin, T. Yamamoto, K. Inomata, Y. Nakamura, and J. S. Tsai, Resonance Fluorescence of a Single Artificial Atom, *Science* **327**, 840 (2010).
- [11] A. A. Abdumalikov, O. V. Astafiev, Y. A. Pashkin, Y. Nakamura, and J. S. Tsai, Dynamics of Coherent and Incoherent Emission from an Artificial Atom in a 1D Space, *Physical Review Letters* **107**, 043604 (2011).
- [12] T. Hönigsl-Deccrinis, R. Shaikhaidarov, S. de Graaf, V. Antonov, and O. Astafiev, Two-Level System as a Quantum Sensor for Absolute Calibration of Power, *Physical Review Applied* **13**, 024066 (2020).
- [13] Y. Lu, A. Bengtsson, J. J. Burnett, E. Wiegand, B. Suri, P. Krantz, A. F. Roudsari, A. F. Kockum, S. Gasparinetti, G. Johansson, and P. Delsing, Characterizing decoherence rates of a superconducting qubit by direct microwave scattering, *npj Quantum Information* **7**, 1 (2021).
- [14] P. Campagne-Ibarcq, P. Six, L. Bretheau, A. Sarlette, M. Mirrahimi, P. Rouchon, and B. Huard, Observing Quantum State Diffusion by Heterodyne Detection of Fluorescence, *Physical Review X* **6**, 011002 (2016).
- [15] A. N. Jordan, A. Chantasri, P. Rouchon, and B. Huard, Anatomy of fluorescence: quantum trajectory statistics from continuously measuring spontaneous emission, *Quantum Studies: Mathematics and Foundations* **3**, 237 (2016).
- [16] P. Campagne-Ibarcq, S. Jezouin, N. Cottet, P. Six, L. Bretheau, F. Mallet, A. Sarlette, P. Rouchon, and B. Huard, Using Spontaneous Emission of a Qubit as a Resource for Feedback Control, *Physical Review Letters* **117**, 060502 (2016).
- [17] M. Naghiloo, N. Foroozani, D. Tan, A. Jadbabaie, and K. W. Murch, Mapping quantum state dynamics in spontaneous emission, *Nature Communications* **7**, 11527 (2016).
- [18] Q. Ficheux, S. Jezouin, Z. Leghtas, and B. Huard, Dynamics of a qubit while simultaneously monitoring its relaxation and dephasing, *Nature Communications* **9**, 1926 (2018).
- [19] P. Campagne-Ibarcq, L. Bretheau, E. Flurin, A. Auffèves, F. Mallet, and B. Huard, Observing Interferences between Past and Future Quantum States in Resonance Fluorescence, *Physical Review Letters* **112**, 180402 (2014).
- [20] D. Tan, N. Foroozani, M. Naghiloo, A. H. Küllerich, K. Mølmer, and K. W. Murch, Homodyne monitoring of postselected decay, *Physical Review A* **96**, 022104 (2017).
- [21] M. Naghiloo, D. Tan, P. M. Harrington, P. Lewalle, A. N. Jordan, and K. W. Murch, Quantum caustics in resonance-fluorescence trajectories, *Physical Review A* **96**, 053807 (2017).
- [22] Supplemental material.
- [23] C. Cohen-Tannoudji, J. Dupont-Roc, and G. Grynberg, *Atom-Photon Interactions: Basic Processes and Applications* (Wiley, 1998).
- [24] P. Bertet, S. Osnaghi, A. Rauschenbeutel, G. Nogues, A. Auffèves, M. Brune, J. M. Raimond, and S. Haroche, A complementarity experiment with an interferometer at the quantum-classical boundary, *Nature* **411**, 166 (2001).
- [25] C. Macklin, K. O'Brien, D. Hover, M. E. Schwartz, V. Bolkhovskiy, X. Zhang, W. D. Oliver, and I. Siddiqi, A near-quantum-limited Josephson traveling-wave parametric amplifier, *Science* **350**, 307 (2015).
- [26] U. Vool and M. Devoret, Introduction to quantum electromagnetic circuits, *International Journal of Circuit Theory and Applications* **45**, 897 (2017).
- [27] A. A. Clerk, M. H. Devoret, S. M. Girvin, F. Marquardt, and R. J. Schoelkopf, Introduction to quantum noise, measurement, and amplification, *Reviews of Mod-*

- ern Physics **82**, 1155 (2010).
- [28] N. Cottet, *Energy and information in fluorescence with superconducting circuits*, PhD Thesis, ENS Paris (2018).
 - [29] H. M. Wiseman, Weak values, quantum trajectories, and the cavity-QED experiment on wave-particle correlation, *Physical Review A* **65**, 032111 (2002).
 - [30] M. Tsang, Optimal waveform estimation for classical and quantum systems via time-symmetric smoothing, *Physical Review A* **80**, 033840 (2009).
 - [31] S. Gammelmark, B. Julsgaard, and K. Mølmer, Past Quantum States of a Monitored System, *Physical Review Letters* **111**, 160401 (2013).
 - [32] M. Maffei, P. A. Camati, and A. Auffèves, Probing non-classical light fields with energetic witnesses in Waveguide Quantum Electro-Dynamics, [arXiv:2102.05941 \[quant-ph\]](#) (2021).
 - [33] M. Maffei et. al., In preparation.
 - [34] J. Dressel, M. Malik, F. M. Miatto, A. N. Jordan, and R. W. Boyd, Colloquium: Understanding quantum weak values: Basics and applications, *Reviews of Modern Physics* **86**, 307 (2014).
 - [35] K. A. Fischer, R. Trivedi, V. Ramasesh, I. Siddiqi, and J. Vučković, Scattering into one-dimensional waveguides from a coherently-driven quantum-optical system, *Quantum* **2**, 69 (2018).
 - [36] J.-C. Besse, S. Gasparinetti, M. C. Collodo, T. Walter, A. Remm, J. Krause, C. Eichler, and A. Wallraff, Parity Detection of Propagating Microwave Fields, *Physical Review X* **10**, 011046 (2020).
 - [37] R. Dassonneville, R. Assouly, T. Peronnin, P. Rouchon, and B. Huard, Number-Resolved Photocounter for Propagating Microwave Mode, *Physical Review Applied* **14**, 044022 (2020).
 - [38] K. Brandner, M. Bauer, M. T. Schmid, and U. Seifert, Coherence-enhanced efficiency of feedback-driven quantum engines, *New Journal of Physics* **17**, 065006 (2015).
 - [39] J. Yi, P. Talkner, and Y. W. Kim, Single-temperature quantum engine without feedback control, *Physical Review E* **96**, 022108 (2017).
 - [40] C. Elouard, D. Herrera-Martí, B. Huard, and A. Auffèves, Extracting Work from Quantum Measurement in Maxwell's Demon Engines, *Physical Review Letters* **118**, 260603 (2017).
 - [41] C. Elouard and A. N. Jordan, Efficient Quantum Measurement Engines, *Physical Review Letters* **120**, 260601 (2018).
 - [42] X. Ding, J. Yi, Y. W. Kim, and P. Talkner, Measurement-driven single temperature engine, *Physical Review E* **98**, 042122 (2018).
 - [43] K. Abdelkhalek, Y. Nakata, and D. Reeb, Fundamental energy cost for quantum measurement, [arXiv:1609.06981 \[cond-mat, physics:quant-ph\]](#) (2018).
 - [44] L. Buffoni, A. Solfanelli, P. Verrucchi, A. Cuccoli, and M. Campisi, Quantum Measurement Cooling, *Physical Review Letters* **122**, 070603 (2019).
 - [45] A. Solfanelli, L. Buffoni, A. Cuccoli, and M. Campisi, Maximal energy extraction via quantum measurement, *Journal of Statistical Mechanics: Theory and Experiment* **2019**, 094003 (2019).
 - [46] C. Elouard, M. Waegell, B. Huard, and A. N. Jordan, An Interaction-Free Quantum Measurement-Driven Engine, *Foundations of Physics* **50**, 1294 (2020).
 - [47] A. N. Jordan, C. Elouard, and A. Auffèves, Quantum measurement engines and their relevance for quantum interpretations, *Quantum Studies: Mathematics and Foundations* **7**, 203 (2020).
 - [48] S. Seah, S. Nimmrichter, and V. Scarani, Maxwell's Lesser Demon: A Quantum Engine Driven by Pointer Measurements, *Physical Review Letters* **124**, 100603 (2020).
 - [49] L. Bresque, P. A. Camati, S. Rogers, K. Murch, A. N. Jordan, and A. Auffèves, Two-Qubit Engine Fueled by Entanglement and Local Measurements, *Physical Review Letters* **126**, 120605 (2021).
 - [50] S. K. Manikandan, C. Elouard, K. W. Murch, A. Auffèves, and A. N. Jordan, Efficiently Fuelling a Quantum Engine with Incompatible Measurements, [arXiv:2107.13234 \[cond-mat, physics:quant-ph\]](#) (2021).

Supplemental Material: Energetics of a Single Qubit Gate

J. Stevens,^{1,*} D. Szombati,^{1,*} M. Maffei,² C. Elouard,³ R. Assouly,¹
 N. Cottet,¹ R. Dassonneville,¹ Q. Ficheux,¹ S. Zeppetzauer,¹
 A. Bienfait,¹ A. N. Jordan,^{4,5} A. Auffèves,² and B. Huard¹

¹*Univ Lyon, ENS de Lyon, CNRS, Laboratoire de Physique, F-69342 Lyon, France*

²*CNRS and Université Grenoble Alpes, Institut Néel, F-38042 Grenoble, France*

³*QUANTIC team, INRIA de Paris, 2 Rue Simone Iff, 75012 Paris, France*

⁴*Institute for Quantum Studies, Chapman University,
 1 University Drive, Orange, CA 92866, USA*

⁵*Department of Physics and Astronomy, University of Rochester, Rochester, New York 14627, USA*

(Dated: September 21, 2021)

I. POST-SELECTED POWER RECORDS

In Fig. S1, we show post-selected power fluorescence for 400 ns long Gaussian edged pulses and for additional varying Rabi frequencies Ω_a which were not shown in Fig. 2 of the main text. We attribute the discrepancy between theory and experiment that occurs in the first 50 ns of the pulse to deformations of the Gaussian edge due to impedance mismatches on the transmission line.

II. HAMILTONIAN OF THE SYSTEM

We consider our system falls under the dispersive approximation, which we can express using the following Hamiltonian:

$$H/\hbar = \omega_R \hat{a}^\dagger \hat{a} + \frac{\omega_Q}{2} \hat{\sigma}_z - \frac{\chi}{2} \hat{a}^\dagger \hat{a} \hat{\sigma}_z + \sqrt{\Gamma_a} \alpha_{\text{in}}(t) \hat{\sigma}_x, \quad (\text{S1})$$

where $\chi = 2\pi \times 4.5$ MHz is the dispersive shift and the last term represents the qubit drive.

III. MEASUREMENT SETUP

The full measurement setup of our experiment is shown in Fig. S2. The microwave pulses driving the qubit and readout are generated by two independent channels in a Tabor WX1284C arbitrary wave generator (AWG) at 100 MHz and 125 MHz respectively. These frequencies are upconverted by double balanced mixers (Marki M1-0412) by mixing the AWG signal with continuous microwave tone local oscillators: an Anapico APSIN12G (qubit drive) and a WindFreak Technologies SynthHD (readout). The local oscillators are split to also provide the references for downconversion.

The readout pulse transmitted through the cavity and the reflected qubit pulse are first amplified at the 15 mK stage by a Travelling Wave Parametric Amplifier (TWPA) provided by Lincoln Labs, before further amplification by a High Electron Mobility Transistor amplifier (HEMT) made by LNF at the 4 K stage. At room temperature, the output channel is split, and downconverted using the two continuous wave local oscillators. The downconversion is performed by image reject mixers (Polyphase IRM4080B for the drive and Marki IRZ0618 for the readout tone). The signals are then digitized using an Alazar acquisition board.

The TWPA itself needs to be driven by a continuous microwave tone for which we use an Anapico APSIN20G.

The cavity total loss rate is $\kappa = 2\pi \times 12$ MHz and the dispersive shift is $\chi = 2\pi \times 4.5$ MHz. The transmon anharmonicity is $\alpha = 2\pi \times 150$ MHz.

* These authors have contributed equally.

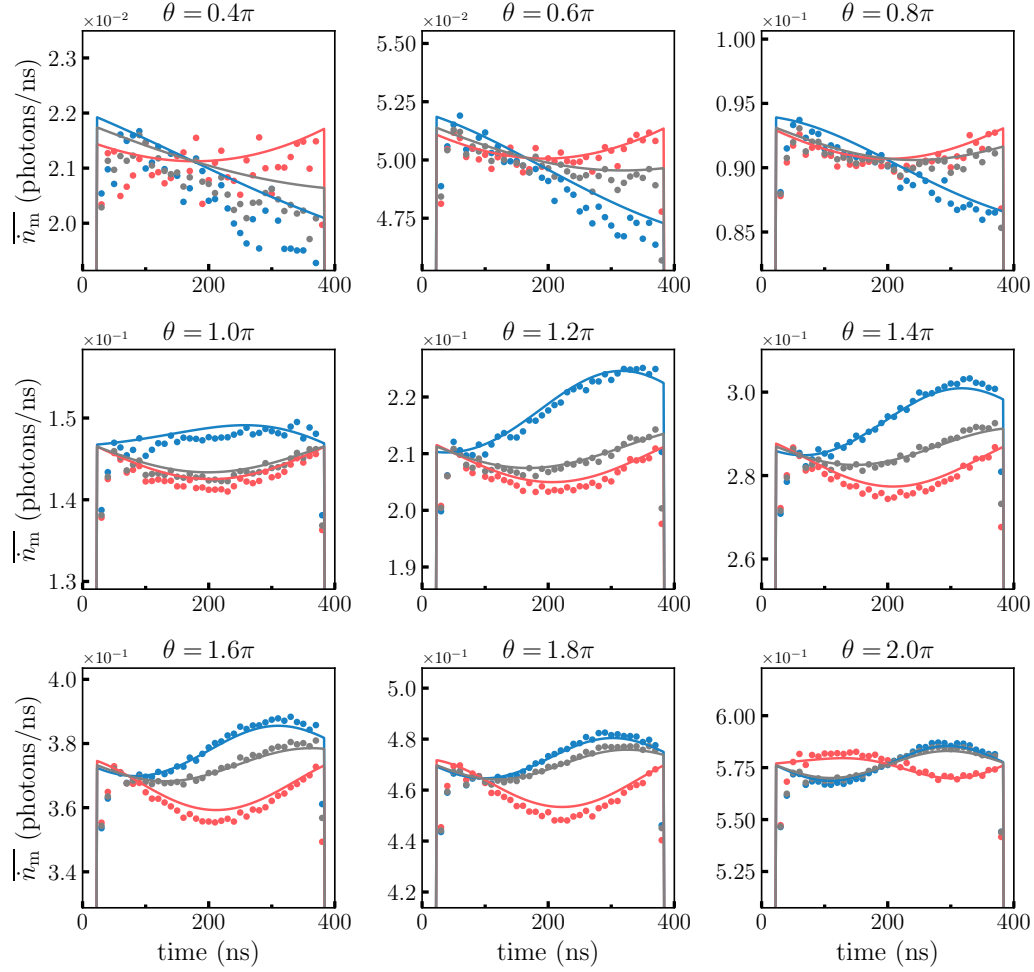


FIG. S1. Measured power of the reflected drive using the same conditions as in Fig. 2 of the main text ($t_d = 400$ ns), but acquired for different drive amplitudes resulting in the qubit rotation angles θ indicated above each subplot. Dots: measured instantaneous power \bar{n}_m of the outgoing drive in units of photon flux (gray: no post-selection, red: post-selected on the qubit being in $|e\rangle$, blue: post-selected for the qubit being in $|g\rangle$). Lines: simulated power as derived in the main text.

IV. PULSE SEQUENCE USED FOR POWER MEASUREMENTS IN THE MAIN TEXT

The full measurement sequence of the experiment is presented in Fig. S3. Initially, a state preparation pulse is sent at the qubit frequency ω_Q for a time t_d and amplitude α_{in} which vary depending on the qubit state we want to prepare. After waiting 20 ns, a square readout pulse of length $t_{RO} = 704$ ns is sent into the cavity. The main role of this pulse consists in realizing the strong measurement of the qubit state on which the drive power measurements are conditioned.

In the experiment, we also used this pulse as part of a monitoring sequence for the qubit relaxation time T_1 . The monitoring is performed by a second readout pulse delayed by a time $t_w = 5$ μ s after the first one. When the first readout pulse projects the qubit onto the state $|x\rangle$, the probability for the qubit to be measured in the same state during the second readout is directly related to T_1

$$p_x(t_w) = (1 - p_x^{\text{th}})e^{-t_w/T_1} + p_x^{\text{th}}. \quad (\text{S2})$$

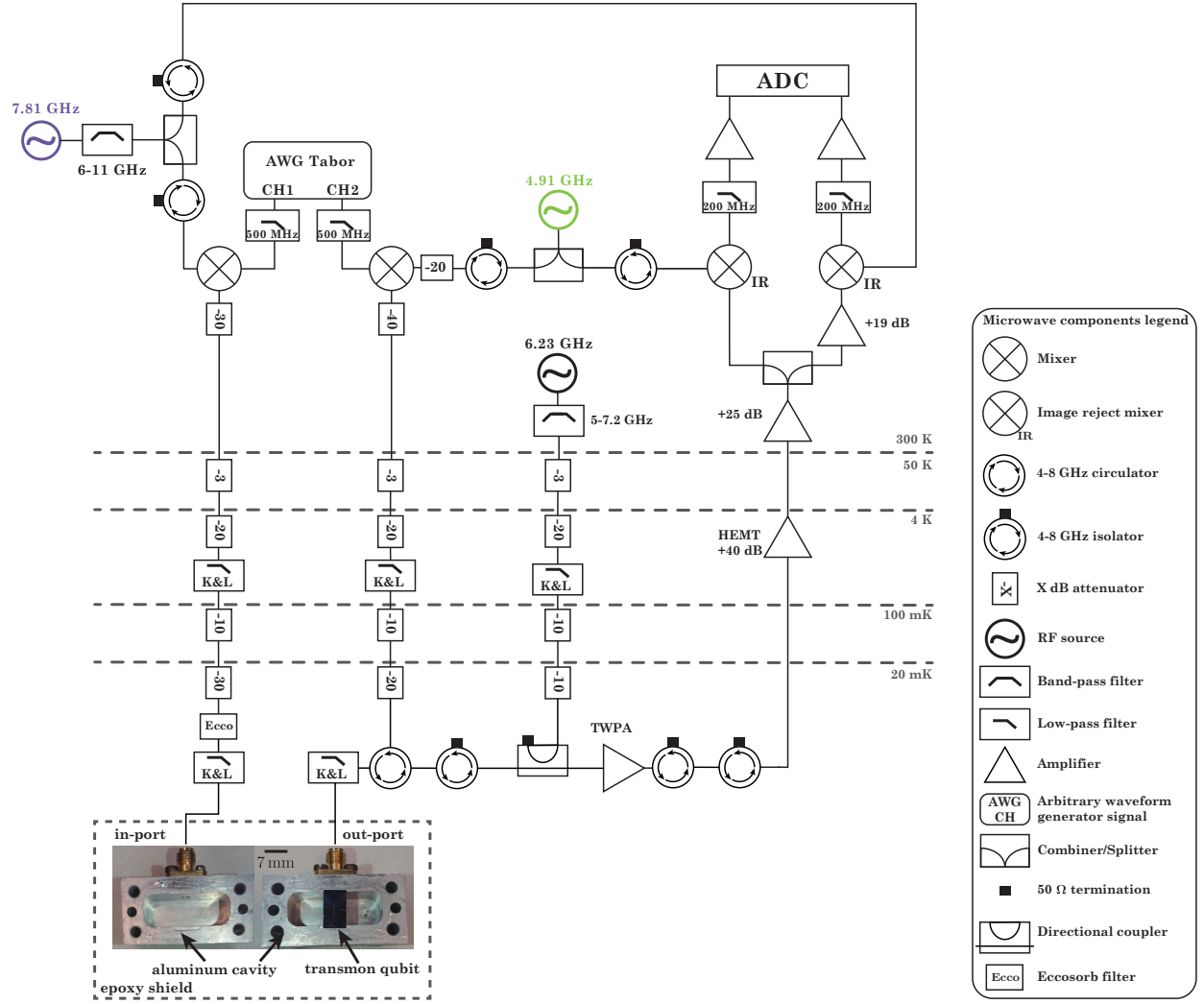


FIG. S2. Schematic of the experiment setup.

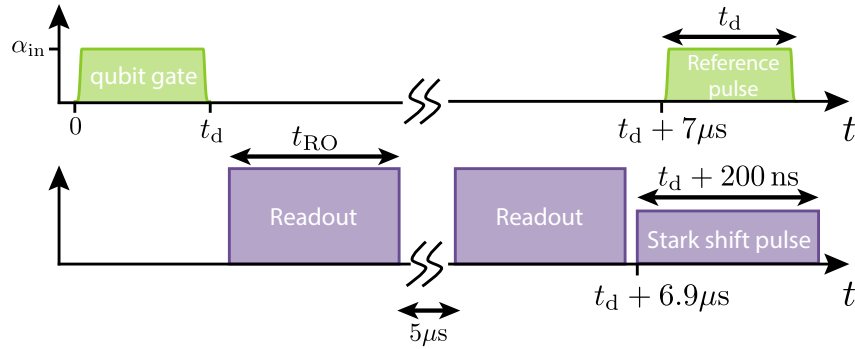


FIG. S3. Full pulse sequence for the experiment. Upper plot and lower plot are the qubit and the readout drive amplitudes respectively. The pulses at the qubit frequency have Gaussian edges (see Eq. (S3)) whereas pulses at the cavity frequency are square.

In Eq. (S2), $p_x^{\text{th}} = \langle x | \rho_{\text{th}} | x \rangle$ is the equilibrium thermal population of state $|x\rangle$ and $p_x(t_w)$ is the probability of finding the qubit in state $|x\rangle$ after the second readout given that it was measured in $|x\rangle$ during the first readout. With all but T_1 known, this allows us to keep track of the average T_1 over the course of the experiment. To eliminate drifts, we create batches of 40000 realizations over which we evaluate T_1 separately. We only keep the batches for which the T_1 time falls within the range $T_1 = 5.5 \pm 0.3 \mu\text{s}$ (which amounts to discarding about 20% of the data).

Finally, in the last part of the pulse sequence, we probe the drive pulse in reflection when the qubit is off resonant. As is explained in Sec. V, the objective is to obtain a reference for the transmission of our lines and for the gain of the amplification chain G which can vary slightly over time. To do so, we simultaneously apply a strong drive at the cavity frequency called the Stark shift pulse and a drive identical to the first qubit gate. The Stark shift pulse shifts the qubit to lower frequencies so that the pulse at ω_Q no longer drives the $|g\rangle - |e\rangle$ transition. We ensure that the cavity drive extends temporally on either side of the qubit drive at ω_Q to be certain that the qubit is far detuned on arrival of the qubit pulse. Additionally, having the cavity pulse turned on while the qubit drive is extinguished allows us to quantify the cross-talk between channels in our acquisition board (see Sec. V), which is needed to estimate the power in our qubit reference drive pulse.

All qubit pulses in the experiment use Gaussian edged square pulses to prevent spectral leakage. The functional describing the pulse envelope is

$$f(t) = \begin{cases} A \exp\left(-\frac{(t-2w)^2}{\frac{2w^2}{8 \ln 2}}\right), & \text{for } t \leq 2w ; \\ A \exp\left(-\frac{(t-t_d+2w)^2}{\frac{2w^2}{8 \ln 2}}\right), & \text{for } t_d - t \leq 2w ; \\ A, & \text{else ;} \end{cases} \quad (\text{S3})$$

where $w = 10 \text{ ns}$ and A is the pulse amplitude.

V. CALIBRATING THE GAIN AND NOISE OF THE MEASUREMENT SETUP

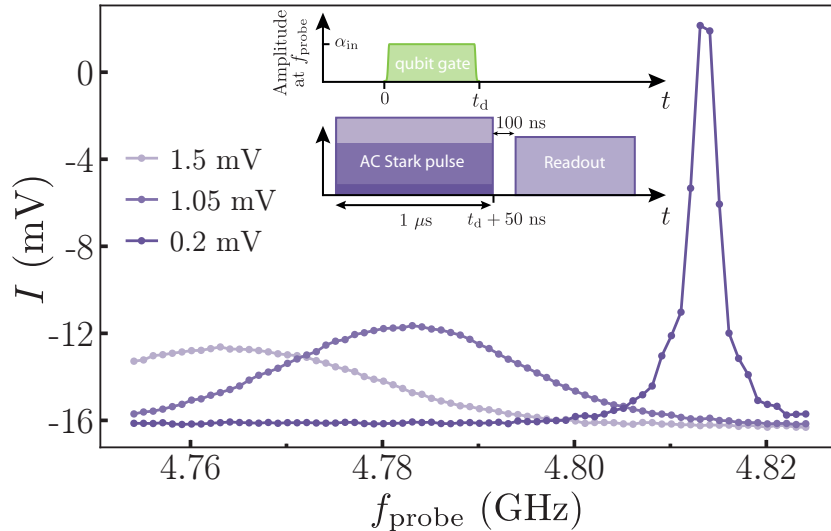


FIG. S4. Average measured readout quadrature during the readout pulse (larger value for larger qubit excitation) as a function of qubit probe frequency f_{probe} for various amplitudes of the AC Stark pulse (colors). The amplitude of the Stark-shift pulse used in the main text (see Fig. S3) is 0.8 mV. Inset: Pulse sequence.

The heterodyne measurement realized at ω_Q in our experimental setup gives us the quadratures I and Q of the reflected qubit pulse after amplification by the readout chain of amplifiers. We

define the measured instantaneous power at ω_Q as $P_{\text{raw}}(t) = (I(t)^2 + Q(t)^2)/Z_0$, where $Z_0 = 50 \Omega$ is the input impedance of our acquisition board.

We wish to relate this quantity to the drive's photon flux outgoing from the cavity (before amplification) $\overline{\dot{n}_m} = \langle \hat{a}_{\text{out}}^\dagger \hat{a}_{\text{out}} \rangle$, where we have defined \hat{a}_{out} as the outgoing drive field operator. We can relate the field after amplification, \hat{b}_{out} , to the outgoing cavity field by [1]

$$\hat{b}_{\text{out}} = \sqrt{G}\hat{a}_{\text{out}} + \sqrt{G-1}\hat{\ell}_{\text{out}}^\dagger, \quad (\text{S4})$$

where $\hat{\ell}_{\text{out}}$ corresponds to the field operator of an effective idler mode, that captures the addition of noise in the quantum-mechanical model of phase-preserving amplification. The power after amplification can then be related to the incoming power $|\alpha_{\text{in}}|^2$ and to the qubit dynamics by

$$\langle \hat{b}_{\text{out}}^\dagger \hat{b}_{\text{out}} \rangle = G \left(|\alpha_{\text{in}}|^2 + \Gamma_a \frac{1 + \langle \hat{\sigma}_z \rangle}{2} - \frac{\Omega_a}{2} \langle \hat{\sigma}_x \rangle \right) + (G-1) \langle \hat{\ell}_{\text{out}}^\dagger \hat{\ell}_{\text{out}} \rangle. \quad (\text{S5})$$

When measuring the power of the outgoing field after amplification $P_{\text{raw}}(t) = \langle \hat{b}_{\text{out}}^\dagger \hat{b}_{\text{out}} \rangle$, it is thus necessary to calibrate both the gain G of the amplifier chain as well as the added noise to calculate $\overline{\dot{n}_m}$. In addition, it is necessary to take into account drifts in gain. Our calibration procedure, involving the measurement of three additional quantities, is as follows:

- The noise power $P_{\text{vac}} = (G-1) \langle \hat{\ell}_{\text{out}}^\dagger \hat{\ell}_{\text{out}} \rangle$ incoming into our acquisition board is acquired with all inputs switched off during some dead time at the beginning of the pulse sequence.
- The reference drive pulse power P_{ref} is measured when the qubit is far detuned from the drive frequency using the AC-Stark shift (see Fig. S4 for the shifted qubit spectrum and Fig. S3 for the pulse sequence). P_{ref} thus corresponds to measuring $G|\alpha_{\text{in}}|^2 + P_c + P_{\text{vac}}$, where P_c is attributed to cross-talk in our acquisition board when the cavity drive is on.
- The crosstalk contribution P_c is estimated by measuring the incoming power $P_c + P_{\text{vac}}$ into our acquisition board when the cavity drive is on but the qubit drive is off.

While P_{raw} is averaged trace by trace, we calculate P_{ref} , P_{vac} and $P_c + P_{\text{vac}}$ by realizing an average over all traces and averaging over all time bins for which the signal amplitude has reached a steady-state. To compensate as much as possible for drifts in gain and phase over time, we acquire 20 batches of one million individual traces. In each batch, we average the four measurements (P_{raw} , P_{ref} , P_{vac} and $P_c + P_{\text{vac}}$), and then use the average quantities in the calculation of $\overline{\dot{n}_m}$, using the following equation

$$\overline{\dot{n}_m}(t) = \frac{\overline{P_{\text{raw}}}(t) - \overline{P_{\text{vac}}}}{G} = \frac{\overline{P_{\text{raw}}}(t) - \overline{P_{\text{vac}}}}{(\overline{P_{\text{ref}}} - \overline{P_c} - \overline{P_{\text{vac}}})/|\alpha_{\text{in}}|^2} = \frac{\Omega_a^2}{4\Gamma_a} \frac{\overline{P_{\text{raw}}}(t) - \overline{P_{\text{vac}}}}{\overline{P_{\text{ref}}} - \overline{P_c} - \overline{P_{\text{vac}}}} \quad (\text{S6})$$

since $|\alpha_{\text{in}}|^2 = \frac{4\Gamma_a}{\Omega_a^2}$. The prefactor $\frac{\Omega_a^2}{4\Gamma_a}$ introduced in Eq. (S6) is measured by two independent measurements: Ω_a by Rabi oscillation measurements, and Γ_a by performing direct spectroscopy of the qubit (see Sec. VI).

Similarly, the reflected pulse amplitude $\overline{\alpha_m}$ can be expressed as

$$\overline{\alpha_m}(t) = \frac{\overline{I}(t) + i\overline{Q}(t)}{\sqrt{G}} = \frac{\Omega_a}{2\sqrt{\Gamma_a}} \frac{\overline{I}(t) + i\overline{Q}(t)}{(\overline{P_{\text{ref}}} - \overline{P_c} - \overline{P_{\text{vac}}})^{1/2}} \quad (\text{S7})$$

VI. DETERMINING THE PURCELL RATE Γ_a

The Purcell rate Γ_a characterizes the relaxation rate of the qubit into the output transmission line. We determine it by measuring the reflection coefficient of the qubit with the output transmission line (Fig. S5) [2]. We drive the qubit at a frequency ω_d for 10 μs , a duration much longer than the Rabi decay time T_R such that the qubit reaches its steady-state. Using the steady-state solution of the Bloch equations [3], and accounting for the qubit thermal population, we find

$$\langle \hat{\sigma}_- \rangle = (p_g^{\text{th}} - p_e^{\text{th}}) \frac{\Omega_a \Gamma_1 (\Gamma_2 - i\delta)}{2[\Gamma_1 (\Gamma_2^2 + \delta^2) + \Gamma_2 \Omega_a^2]}, \quad (\text{S8})$$

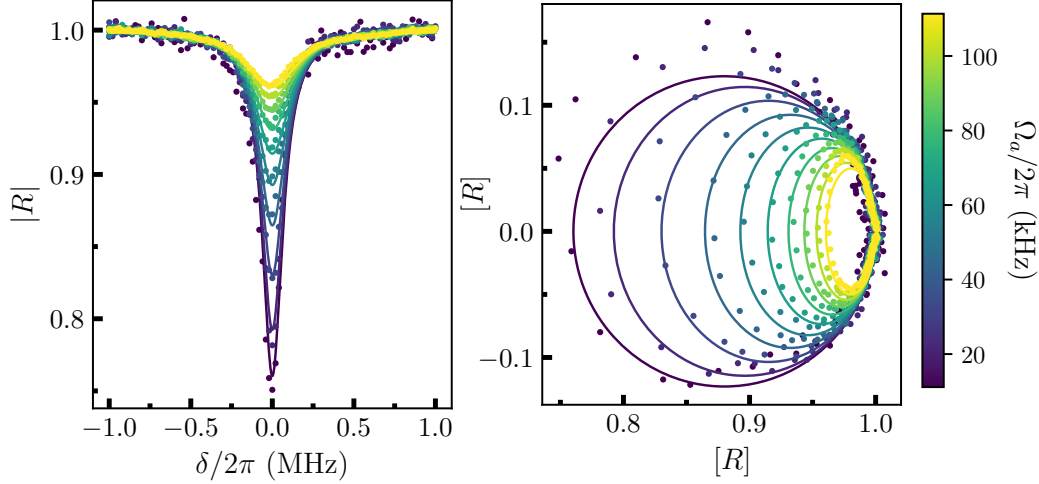


FIG. S5. (a) Dots: Measured amplitude of the reflection coefficient on the output as a function of detuning δ between the drive and the qubit frequency for various drive amplitudes. Lines: amplitude of Eq. (S9) plotted with the fit parameters $\Gamma_a/2\pi \approx 20$ kHz and Ω_a given in the color bar. (b) Same measurement and prediction shown as parametric plots in the complex plane.

where $\Gamma_1 = 1/T_1$, $\Gamma_2 = 1/T_2$, $\delta = \omega_Q - \omega_d$. The thermal populations p_g^{th} and p_e^{th} are determined by the relative weights of the Gaussian fit to a readout histogram with the qubit in the thermal state (see section VII), and T_1 and T_2 are measured using standard relaxation and Ramsey interferometry techniques. The reflection coefficient $R = \frac{\langle \hat{a}_{\text{out}} \rangle}{\langle \hat{a}_{\text{in}} \rangle}$ is given by

$$R = 1 - (p_g^{\text{th}} - p_e^{\text{th}}) \frac{\Gamma_a \Gamma_1 (\Gamma_2 - i\delta)}{[\Gamma_1 (\Gamma_2^2 + \delta^2) + \Gamma_2 \Omega_a^2]} . \quad (\text{S9})$$

While the amplification chain introduces a scaling factor between the fields $\langle \hat{a}_{\text{out}} \rangle$, $\langle \hat{a}_{\text{in}} \rangle$ and the fields that we actually measure, it can be taken into account by measuring R for large detuning δ . This leaves Ω_a and Γ_a as the only fit parameters in Eq. S9. We show $R(\delta)$ for various Rabi frequencies Ω_a in Fig. S5, from which we extract $\Gamma_a/2\pi \approx 20$ kHz.

VII. ANALYZING THE READOUT HISTOGRAMS

Outgoing signals from the experiment are digitized and numerically demodulated to extract their I and Q quadratures. For the readout pulse, the quadratures are defined as

$$I = \frac{1}{t_{\text{RO}}} \int_0^{t_{\text{RO}}} V_{\text{out}}(t) \cos(\omega_{\text{IF}} t) dt , \quad (\text{S10})$$

$$Q = \frac{1}{t_{\text{RO}}} \int_0^{t_{\text{RO}}} V_{\text{out}}(t) \sin(\omega_{\text{IF}} t) dt , \quad (\text{S11})$$

where $\omega_{\text{IF}}/2\pi$ is the AWG modulation frequency and $V_{\text{out}}(t)$ is the voltage recorded by the ADC. A histogram of recorded values of $I + iQ$ for 40000 readout pulses is shown in Fig. S6a. By using a Gaussian mixture model (GMM) [4] on the distribution of measured $I + iQ$ values, we can fit three Gaussian distributions in the quadrature phase space, which we identify with the qubit being in states $|g\rangle$, $|e\rangle$ or $|f\rangle$. This divides the IQ plane into three regions of the phase space (labeled “G”, “E” and “F”), such that the region in which a measurement outcome is located indicates that the qubit is most likely in $|g\rangle$, $|e\rangle$ or $|f\rangle$. The resulting segmentation and the distribution of recorded points in the complex plane are shown in Fig. S6b.

The GMM algorithm directly gives the weights of the Gaussian distributions most likely to reproduce the histograms obtained from the readout quadratures. We identify these weights with

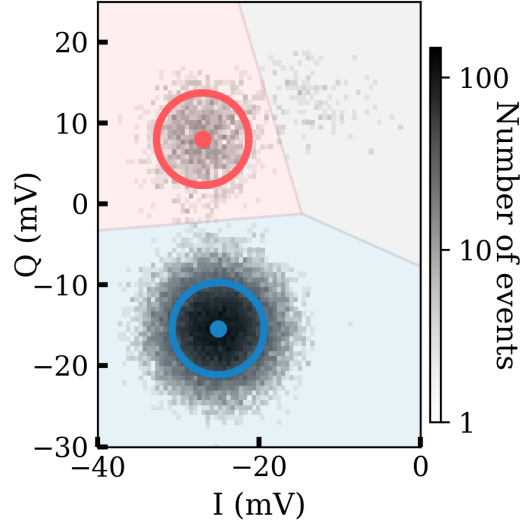


FIG. S6. Histogram of 40000 measured quadratures (I, Q) of the readout pulse when the qubit is at thermal equilibrium. The three visible Gaussian peaks correspond to the qubit being in $|g\rangle$, $|e\rangle$ and $|f\rangle$ states. Dots: Mean of the Gaussian distributions (blue when the qubit is in $|g\rangle$, red when in $|e\rangle$). Circles: contours of the Gaussian distributions at $1.5\sigma_{IQ}$. The plane is segmented into three sectors “G”, “E” and “F” (blue, red and gray coloring respectively) according to the Gaussian mixture model [4].

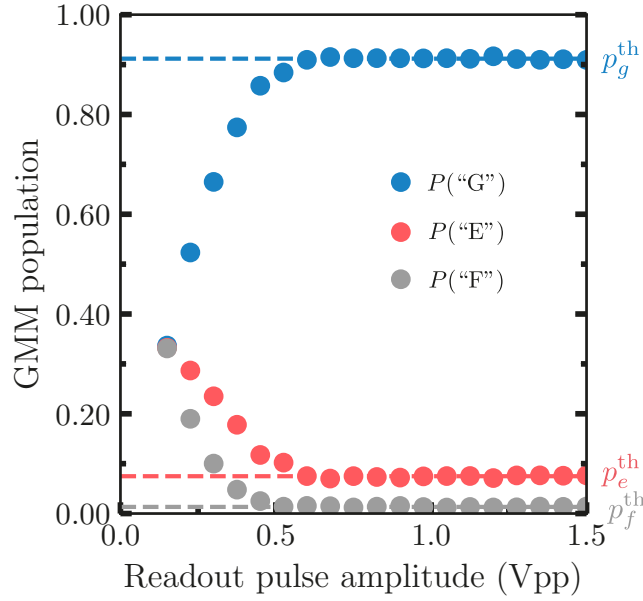


FIG. S7. Extracted populations of each qubit state using the GMM algorithm as a function of the readout pulse amplitude in units of the IF voltage on the room temperature mixer.

the transmon population of its three lowest energy states immediately before the readout. We can use this measurement to determine the qubit thermal population. In Fig. S7, we show the qubit populations as a function of the readout pulse amplitude. At low amplitude, the measurement is very imprecise, as the pointer states of the readout are not fully separated yet, explaining the change in population below an amplitude of 0.5Vpp. At higher amplitudes, the populations do not change with the readout amplitude, indicating that the amplitude of the readout pulse has no effect on the observed qubit populations.

To calibrate the thermal populations used for the fits in the main text, we run the GMM

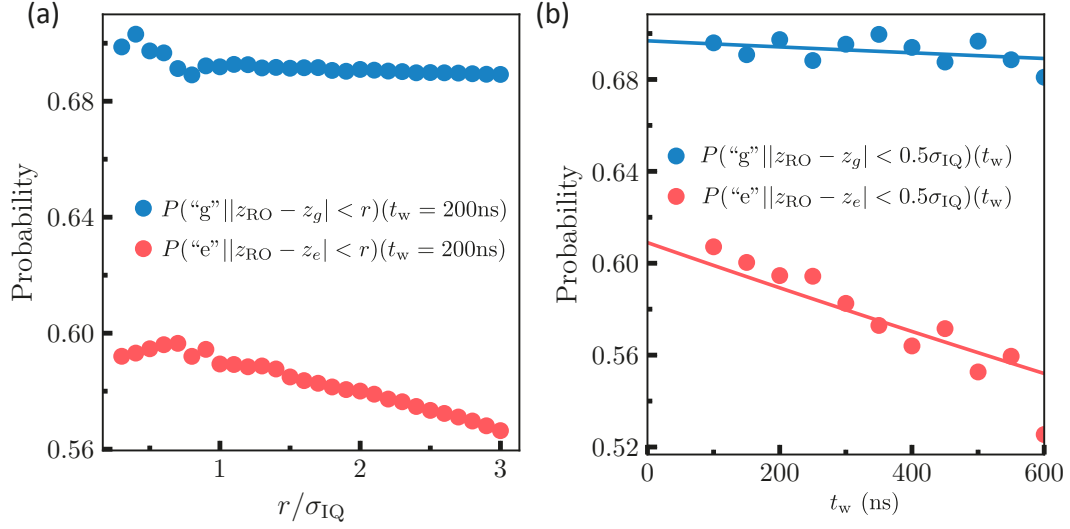


FIG. S8. (a) Dependence on r of the measured probability $P(\text{"x"} | |z_{\text{RO}} - z_g| < r)$ of finding the outcome "x" during the second readout pulse knowing that a first readout pulse, ending 200 ns earlier, gave a measured amplitude $I + iQ$ that is closer than r to the average amplitude z_x associated with $|x\rangle$ (dot in Fig. S6). (b) Dependence on the waiting time t_w between the two readout pulses of the probability of obtaining the measurement outcome "x" in the second readout, given the measured amplitude during the first measurement lies within distance $0.5\sigma_{\text{IQ}}$ from z_x ($x \in \{g, e\}$). The solid lines are given by Eq. (S15) with $T_1 = 5.5\mu\text{s}$, $p_g^{\text{th}} = 0.892$ and $p_e^{\text{th}} = 0.088$, $P(\text{"g"} | |g\rangle) = 0.696$, $P(\text{"e"} | |e\rangle) = 0.605$ and $P(\text{"g"} | |e\rangle) = P(\text{"e"} | |g\rangle) = 0$.

algorithm on a large set of readout values (930000) taken at large readout amplitude. We extract $p_g^{\text{th}} = 0.892 \pm 0.002$, $p_e^{\text{th}} = 0.088 \pm 0.002$ and $p_f^{\text{th}} = 0.02 \pm 0.002$.

VIII. DATA POST-SELECTION PROTOCOL AND ASSOCIATED READOUT FIDELITY

In the main text, the measured instantaneous power emitted by the qubit is post-selected conditionally on the measurement outcome of each projective readout of the qubit. In order to lower the number of realizations where this projective readout is erroneous, we reject measurement outcomes lying in the region of overlap between different qubit states in the quadrature phase space (we thus reject $\approx 40\%$ of the total number of realizations). It is crucial to carefully assess the resulting readout fidelity since it has a significant impact on the post-selected averages and on the effect matrix.

We now describe the post-selection protocol, and the evaluation of readout fidelities. For the sake of readability, we only describe the method used for post-selected outcomes "g". The derivation for outcome "e" is similar.

The outcome "g" is defined by a measured amplitude $z_{\text{RO}} = I + iQ$ that lies within a distance $1.5\sigma_{\text{IQ}}$ of the centre z_g of the Gaussian distribution corresponding to the pointer-state of $|g\rangle$ (within the blue circle in Fig. S6), with σ_{IQ} the standard deviation of the distributions. The readout fidelity F_g is defined as the probability of being in state $|g\rangle$ at the beginning of the readout pulse, given that the integrated readout record yields the outcome "g". To determine the fidelity F_g , we use Bayes' rule

$$F_g \equiv P(|g\rangle | \text{"g"}) = \frac{P(\text{"g"} | |g\rangle)P(|g\rangle)}{P(\text{"g"})}, \quad (\text{S12})$$

where $P(|g\rangle)$ is the probability of the qubit being in state $|g\rangle$ immediately before the readout, $P(\text{"g"})$ is the probability of obtaining measurement outcome "g", and $P(\text{"g"} | |g\rangle)$ is the probability that the readout outcome is "g", knowing the qubit started in state $|g\rangle$ at the beginning of the

readout. In the formula above, we can evaluate $P(|g\rangle)$ as the probability of the IQ measurement being in sector “G”, as determined by the Gaussian mixture classifier algorithm (see Fig. S6b). On the other hand, $P(\text{“g”})$ is simply the probability of the IQ measurement being in the circle described above. The only term left to determine is the conditional probability $P(\text{“g”} | |g\rangle)$. We measure it using a calibration sequence comprising two readout pulses separated by a tunable waiting time t_w . Two experimental errors need to be taken into account: the ability to determine the outcome of the first measurement, and the relaxation of the qubit during the waiting time.

To minimize the uncertainty in determining the state of the qubit following the first pulse, we optimize the radius r of the circle around z_g in which we consider the qubit to be in $|g\rangle$. Ideally, in order to label the outcome of this first readout pulse, we would consider an infinitely small radius $r \rightarrow 0$. In practice, in Fig. S8a, we plot the conditional probability $P(\text{“g”} | |z_{RO} - z_g| < r)$ for varying r : this is the probability that the outcome of the second readout pulse lies in the circle “g”, given the outcome of the first readout pulse is within the circle of radius r . We observe that this probability saturates as r decreases, such that at sufficiently small r (we take $r < 0.5\sigma_{IQ}$) we can indeed consider the qubit state to have remained in $|g\rangle$ throughout the entire integration time and give an accurate determination for $P(\text{“g”} | |g\rangle)(t_w)$.

Second, we plot $P(\text{“g”} | |g\rangle)(t_w)$ as a function of waiting time t_w in Fig. S8b. We observe that the conditional probability decreases with t_w due to the qubit decaying. This can be accounted for by considering the qubit thermal population and its relaxation rate. Assuming the qubit starts in $|g\rangle$, as ensured by the first readout pulse, the qubit finds itself in the mixed state

$$\rho = p_g(t_w) |g\rangle \langle g| + (1 - p_g(t_w)) |e\rangle \langle e| , \quad (\text{S13})$$

after a waiting time t_w , where

$$p_g(t) = (1 - p_g^{\text{th}})e^{-t/T_1} + p_g^{\text{th}} . \quad (\text{S14})$$

The conditional probability of the outcome “g” for this mixed state is thus given by

$$P(\text{“g”} | |g\rangle)(t_w) = p_g(t_w)P(\text{“g”} | |g\rangle)(t_w = 0) + (1 - p_g(t_w))P(\text{“g”} | |e\rangle)(t_w = 0) . \quad (\text{S15})$$

By adjusting the model of Eq. (S15) we identify the two free parameters $P(\text{“g”} | |g\rangle) = 0.696 \pm 0.002$ and $P(\text{“g”} | |e\rangle) < 10^{-7}$ (T_1 , p_g^{th} and p_e^{th} are measured independently, see Sections IV and VII). The latter value can be explained by the large $6\sigma_{IQ}$ separation between the two pointer states in the quadrature phase space. From these values, and using Eq. (S12) we obtain a fidelity $F_g = 98.5 \pm 1.5\%$.

Using an identical method, we obtain $P(\text{“e”} | |e\rangle) = 0.605 \pm 0.002$ and $P(\text{“e”} | |g\rangle) < 10^{-7}$ and $F_e = 86.7 \pm 2.8\%$.

IX. WEAK VALUES OF THE QUBIT OPERATORS

In this section, we explain how we have modeled the evolution of the qubit and computed the density and effect matrices to fit the instantaneous and average powers we display in Fig. 2 and 3 of the main text.

We model the qubit dynamics using a Lindblad equation [5]. We consider two decoherence channels: pure dephasing at a rate Γ_ϕ , and energy relaxation at a rate Γ_1 that includes radiative relaxation into the output transmission line at a rate Γ_a . To take into account the non-zero temperature of the qubit, we introduce two energy excitation and de-excitation rates Γ_\uparrow and Γ_\downarrow defined as $\Gamma_\uparrow = \frac{p_e^{\text{th}}}{p_g^{\text{th}} + p_e^{\text{th}}} \Gamma_1$ and $\Gamma_\downarrow = \frac{p_g^{\text{th}}}{p_g^{\text{th}} + p_e^{\text{th}}} \Gamma_1$. The Lindblad equation for the density matrix ρ of the qubit can then be written

$$\frac{\partial \rho}{\partial t} = -\frac{i}{\hbar}[H, \rho] + \frac{\Gamma_\phi}{2}D[\hat{\sigma}_z](\rho) + \Gamma_\downarrow D[\hat{\sigma}_-](\rho) + \Gamma_\uparrow D[\hat{\sigma}_+](\rho) , \quad (\text{S16})$$

where the Lindblad superoperator is defined as

$$D[L](\rho) = L\rho L^\dagger - \frac{1}{2}\rho L^\dagger L - \frac{1}{2}L^\dagger L\rho . \quad (\text{S17})$$

The effect matrix E , introduced in Refs. [6–8] propagates the information we have about the qubit at time t backwards in time. It follows similar time dynamics to the density matrix:

$$\frac{\partial E}{\partial t} = -\frac{i}{\hbar}[H, E] - \frac{\Gamma_\phi}{2}D^*[\hat{\sigma}_z](E) - \Gamma_\downarrow D^*[\hat{\sigma}_-](E) - \Gamma_\uparrow D^*[\hat{\sigma}_+](E), \quad (\text{S18})$$

where the adjoint of the Lindblad superoperator is given by

$$D^*[L](E) = L^\dagger E L - \frac{1}{2}E L^\dagger L - \frac{1}{2}L^\dagger L E. \quad (\text{S19})$$

From the past quantum state formalism [6–8], we can predict the expectation value of a qubit operator \hat{O} at time t with the knowledge of its initial state and the outcome of a measurement at a future time t_d using the density and effect matrices. The main result of this weak value formalism is

$${}_{E(t)}\langle \hat{O} \rangle_{\rho(t)} = \frac{\text{Tr}[E(t)\hat{O}\rho(t)]}{\text{Tr}[E(t)\rho(t)]}, \quad t \in [0, t_d]. \quad (\text{S20})$$

We stress that $E(t)$ encapsulates information about the what will occur to the qubit after time t . Thus if at time t_d the measurement of the qubit state yielded outcome “e”, the effect matrix at this time would be given by

$$E(t_d) = F_e |e\rangle \langle e| + (1 - F_e) |g\rangle \langle g|, \quad (\text{S21})$$

where F_e is the readout fidelity defined in section VIII.

X. DEEPER ANALYSIS OF THE TOY MODEL

A. Derivation of the measurement operators

In order to justify the toy model given in the text, let us consider a simple coupling Hamiltonian between the harmonic oscillator a and the qubit in the interaction picture with respect to the free qubit and oscillator

$$H = i\hbar\gamma(a\sigma_+ - a^\dagger\sigma_-). \quad (\text{S22})$$

The stationary coupling constant γ is linked to the qubit interaction rate and the pulse duration by $\gamma = \sqrt{\Gamma_a}/t_d$.

The corresponding unitary operator after a coupling time t_d reads

$$U(t_d) = \cos(\gamma t_d \sqrt{a^\dagger a + 1}) |e\rangle \langle e| + \cos(\gamma t_d \sqrt{a^\dagger a}) |g\rangle \langle g| \quad (\text{S23})$$

$$+ \frac{\sin(\gamma t_d \sqrt{a^\dagger a + 1})}{\sqrt{a^\dagger a + 1}} a \sigma_+ - \frac{\sin(\gamma t_d \sqrt{a^\dagger a})}{\sqrt{a^\dagger a}} a^\dagger \sigma_- \quad (\text{S24})$$

Therefore, when the qubit starts in $|g\rangle$ before the interaction is turned on, the measurement operators corresponding to the qubit measurement outcomes g or e are

$$\hat{M}_g = \langle g|U(t_d)|g\rangle = \cos(\gamma t_d \sqrt{a^\dagger a}) \quad (\text{S25})$$

and

$$\hat{M}_e = \langle e|U(t_d)|g\rangle = \frac{\sin(\gamma t_d \sqrt{a^\dagger a + 1})}{\sqrt{a^\dagger a + 1}} a = \sin(\gamma t_d \sqrt{a^\dagger a + 1}) \hat{e} = \hat{e} \sin(\gamma t_d \sqrt{a^\dagger a}) \quad (\text{S26})$$

Therefore, when starting from an oscillator in state $|\psi\rangle = \sum_{n \geq 0} c_n |n\rangle$, the probability to find the qubit in g is $\langle \psi | \hat{M}_g^\dagger \hat{M}_g | \psi \rangle = \sum_{n \geq 0} |c_n|^2 \cos^2(\gamma t_d \sqrt{n})$ and in e is $\langle \psi | \hat{M}_e^\dagger \hat{M}_e | \psi \rangle = \sum_{n \geq 0} |c_n|^2 \sin^2(\gamma t_d \sqrt{n})$. Finally, the state becomes

$$|\psi_g\rangle = \sum_{n \geq 0} c_n \cos(\gamma t_d \sqrt{n}) |n\rangle \text{ if the outcome is } g \quad (\text{S27})$$

$$|\psi_e\rangle = \sum_{n \geq 1} c_n \sin(\gamma t_d \sqrt{n}) |n-1\rangle \text{ if the outcome is } e. \quad (\text{S28})$$

B. Thermodynamical analysis of another toy experiment – a photodetector on a cavity

It is worth considering the implications of a photodetection event at the port of a cavity to shed light on the thermodynamics of our weak measurement by a qubit. This discussion can be found in the book [9].

Consider a cavity in state $|\psi\rangle = \sum_{n \geq 0} c_n |n\rangle$ that is coupled to a transmission line at a rate κ . An ideal photodetector is connected to that line and the measurement operator associated with a click is $\hat{M}_{\text{click}} = \sqrt{\kappa}a$. The measurement postulate states that when a click occurs, the cavity state becomes

$$|\psi_{\text{click}}\rangle = \hat{M}_{\text{click}}|\psi\rangle / \sqrt{\langle\psi|\hat{M}_{\text{click}}^\dagger \hat{M}_{\text{click}}|\psi\rangle}.$$

From a thermodynamics point of view, we focus on the distribution of photon numbers in the cavity. Quantum theory directly predicts the final photon number distribution

$$\mathbf{P}(n|\text{“click” has occurred}) = |\langle n|\psi_{\text{click}}\rangle|^2 = |c_n|^2 = \frac{|c_{n+1}|^2(n+1)}{\sum_k |c_k|^2 k}.$$

Yet it is interesting to consider a Bayesian analysis of this measurement backaction if one is interested in the thermodynamics of the detector as well. Indeed, where does the energy extracted by the detector appear in this expression?

To answer this question, one can decompose the backaction of a click on the photon number distribution in two steps.

1. Since the probability that a click occurred depends on the number of photons in the cavity (it is linear in n), the fact that a click occurred modifies our knowledge about the number of photons in the cavity. Concretely, a Bayesian analysis provides the probability that the cavity had n photons knowing that a click is bound to occur over the following measurement time τ

$$\mathbf{P}(n|\text{“click” will occur}) = \frac{\mathbf{P}(\text{“click” will occur}|n)\mathbf{P}(n)}{\mathbf{P}(\text{“click” will occur})}. \quad (\text{S29})$$

2. If a photon was photodetected, it has left the cavity to excite the detector by one quantum, and we need to reduce the number of excitations we expect in the cavity by 1

$$\mathbf{P}(n|\text{“click” has occurred}) = \mathbf{P}(n+1|\text{“click” will occur}). \quad (\text{S30})$$

We can calculate these quantities for a click occurring over an observation time window τ :

$$\mathbf{P}(\text{“click” will occur}|n) = \tau \langle n|\hat{M}_{\text{click}}^\dagger \hat{M}_{\text{click}}|n\rangle = n\kappa\tau \quad (\text{S31})$$

$$\mathbf{P}(n) = |\langle n|\psi\rangle|^2 = |c_n|^2 \quad (\text{S32})$$

$$\mathbf{P}(\text{“click” will occur}) = \tau \langle \hat{M}_{\text{click}}^\dagger \hat{M}_{\text{click}} \rangle_{|\psi\rangle} = \kappa\tau \sum_k |c_k|^2 k. \quad (\text{S33})$$

Therefore,

$$\mathbf{P}(n|\text{“click” will occur}) = \frac{|c_n|^2 n}{\sum_k |c_k|^2 k}$$

and we recover the result from the measurement postulate

$$\mathbf{P}(n|\text{“click” has occurred}) = \frac{|c_{n+1}|^2(n+1)}{\sum_k |c_k|^2 k} \quad (\text{S34})$$

It is interesting to apply these considerations in two particular cases.

1. Fock state

If the cavity starts in Fock state $|m\rangle$, step 1 does not change the probability distribution at all and $\mathbf{P}(n|\text{“click” will occur}) = \mathbf{P}(n)$. However, step 2 changes the Fock state from $|m\rangle$ to $|m-1\rangle$ (note that $m \geq 1$ since a click never happens if $m = 0$). This is the simplest case where the entire energy change in the oscillator corresponds to the energy extracted by the detector. But it is by no means general as can be seen in the following second case.

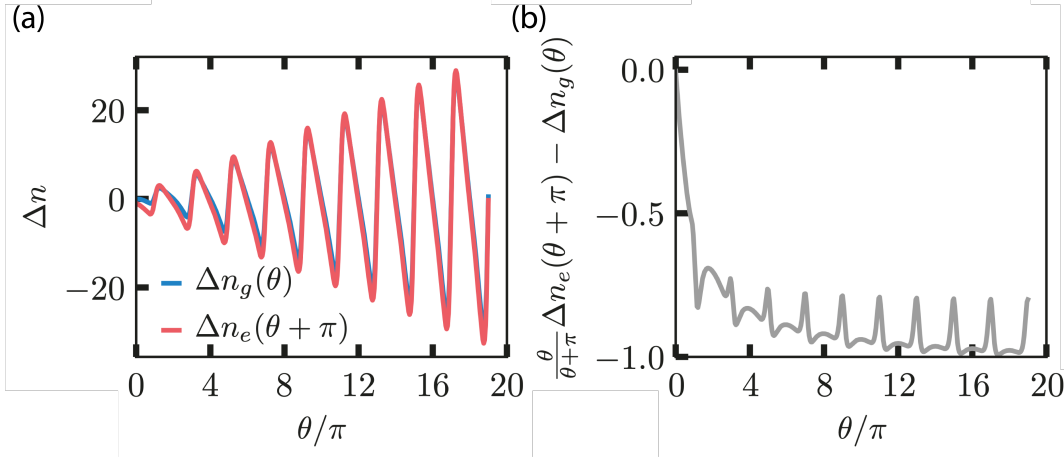


FIG. S9. (a) Comparison of the photon number differences $\Delta n_{g,e}$ for post-selection in “g” and “e” according to the weak value predictions of Eq. (6) of the main text for our experiment. The curve Δn_e is phase shifted by an angle π to highlight the similarity between the two cases up to a half period. (b) Difference between the phase shifted and rescaled Δn_e and Δn_g . For large angle θ , $\frac{\theta}{\theta+\pi} \Delta n_e$ and Δn_g tend to differ by a single excitation corresponding to step 2.

2. Coherent state

If the cavity starts in a coherent state $|\alpha\rangle$, step 1 shifts the Poisson distribution by exactly +1 photon, meaning that detecting a photon informs the observer that there was likely one more photon than anticipated: $\mathbf{P}(n|\text{“click” will occur}) = \mathbf{P}(n-1)$. Then, the extracted photon that is consumed by the photodetector lowers this expectation by 1 so that the final probability is back to the initial one: $\mathbf{P}(n|\text{“click” has occurred}) = \mathbf{P}(n) = \bar{n}^n e^{-\bar{n}}/n!$. The Poisson distribution has the unique property of perfectly compensating the two thermodynamic updates inferred from the measurement.

C. Toy model of the main text – a qubit coupled to a harmonic oscillator

In the main text, the two steps of the previous section are detailed in the case where the oscillator interacts with a qubit that is measured projectively. How does the consumed photon in step 2 manifest itself in the change of photon number predicted by the weak value expression (6) in the main text? We compared the phase shifted photon number differences $\Delta n_g(\theta)$ and $\Delta n_e(\theta + \pi)$ calculated both using Eq. (6) of the main text in Fig. S9a. There is a visible symmetry between the energy changes corresponding to measurement outcomes $|g\rangle$ and $|e\rangle$. They almost perfectly match each other once one of them is shifted by an angle π on the Bloch sphere. They do not overlap perfectly though, because an extra π rotation requires extra photons in the field. Since the backaction experimentally and numerically scales as $\sqrt{n_{\text{in}}} \propto \theta$, it is thus judicious to compare $\Delta n_g(\theta)$ with $\Delta n_e(\theta + \pi)$ rescaled by a factor $\frac{\theta}{\theta+\pi}$ to take the additional rotation into account. The difference $\frac{\theta}{\theta+\pi} \Delta n_e(\theta + \pi) - \Delta n_g(\theta)$ is shown in Fig. S9. For large θ the difference tends to -1. This corresponds to the single photon absorbed by the qubit from the field when it is measured in $|e\rangle$, which is precisely the backaction of step 2. It thus seems possible to separate both contributions to the measurement backaction: the Bayesian update and the energy update due to the detector consumption.

-
- [1] A. A. Clerk, M. H. Devoret, S. M. Girvin, F. Marquardt, and R. J. Schoelkopf, Introduction to quantum noise, measurement, and amplification, *Reviews of Modern Physics* **82**, 1155 (2010).
 - [2] N. Cottet, H. Xiong, L. B. Nguyen, Y.-H. Lin, and V. E. Manucharyan, Electron shelving of a superconducting artificial atom, *arXiv:2008.02423 [cond-mat, physics:quant-ph]* (2020).

- [3] Y. Lu, A. Bengtsson, J. J. Burnett, E. Wiegand, B. Suri, P. Krantz, A. F. Roudsari, A. F. Kockum, S. Gasparinetti, G. Johansson, and P. Delsing, Characterizing decoherence rates of a superconducting qubit by direct microwave scattering, [npj Quantum Information](#) **7**, 1 (2021).
- [4] F. Pedregosa, G. Varoquaux, A. Gramfort, V. Michel, B. Thirion, O. Grisel, M. Blondel, P. Prettenhofer, R. Weiss, V. Dubourg, J. Vanderplas, A. Passos, D. Cournapeau, M. Brucher, M. Perrot, and E. Duchesnay, Scikit-learn: Machine Learning in Python, [Journal of Machine Learning Research](#) **12**, 2825 (2011).
- [5] G. Lindblad, On the generators of quantum dynamical semigroups, [Communications in Mathematical Physics](#) **48**, 119 (1976).
- [6] H. M. Wiseman, Weak values, quantum trajectories, and the cavity-QED experiment on wave-particle correlation, [Physical Review A](#) **65**, 032111 (2002).
- [7] M. Tsang, Optimal waveform estimation for classical and quantum systems via time-symmetric smoothing, [Physical Review A](#) **80**, 033840 (2009).
- [8] S. Gammelmark, B. Julsgaard, and K. Mølmer, Past Quantum States of a Monitored System, [Physical Review Letters](#) **111**, 160401 (2013).
- [9] S. Haroche and J.-M. Raimond, *Exploring the Quantum. Atoms, Cavities and Photons.*, oxford graduate texts ed. (Oxford University Press, 2006).